


Application of the numerical simulation method for the strength analysis of long-term portal crane components

Sebastian Lipiec^{1*} , Olha Zvirko², Ihor Dzioba¹, Oleh Venhryniuk²

¹ Faculty of Mechatronics and Mechanical Engineering, Kielce University of Technology, Av. 1000-An. of Polish State 7, 25-314 Kielce, Poland

² Karpenko Physico-Mechanical Institute of the NAS of Ukraine, Department of Diagnostics of Materials Corrosion-Hydrogen Degradation, 5 Naukova St., Lviv 79060, Ukraine

* Corresponding auth's e-mail: slipiec@tu.kielce.pl

ABSTRACT

In this paper, the strength analysis of the material from two elements of a portal crane operated for about 33 years was carried out. The assessment was based on modelling and numerical simulation results using the finite element method of the load of three-point bending specimens. The constitutive relationships of the materials in the form of true stress-strain relationships were defined based on data from the uniaxial tensile test of the appropriate specimens. The iterative fitting method of the experimental and numerical relationship and the method that considers triaxiality and the Lode parameter were used. The accuracy of the defined stress-strain relationships was verified by comparing the load curves determined experimentally and numerically. Numerical modelling and simulation of the load of three-point bending specimens allowed obtaining stress distributions before the crack tip and the values of fracture toughness – J -integral. The results of the numerically calculated J -integral are similar to the experimental results. The trends in the stress component distributions indicate a high level of fracture toughness of the tested materials, ensuring a ductile nature of subcritical crack growth. The proposed methodology can be applied to other steels of operated structures.

Keywords: portal crane, steel, finite element method, true stress-strain relationship, stress distribution; J -integral.

INTRODUCTION

Engineering structures undergo long-term operation and experience degradation of their microstructure and mechanical properties. The degree and dynamics of this deterioration are influenced by operating conditions, including environmental factors (1–5), temperature (6–8), and other variables (9–17). Consequently, it is necessary to implement strength analyses to assess the condition of an object or engineering element.

In the case of strength analyses of engineering elements, it is possible to use a variety of testing methods. These can consist of tests done directly on the evaluated object, using non-destructive techniques, such as ultrasonic and electromagnetic acoustic signals, etc. (18–22). If it is feasible to extract specimens from an engineering

component for testing, uniaxial tensile, fracture toughness, and/or fatigue tests should be realized (2, 9, 21, 23, 24). Performing experiments in a laboratory makes it possible to obtain information about the basic characteristics of the material from the engineering component under consideration and then perform strength analysis.

An important tool that has already become an everyday reality for engineers and scientists involved in strength analysis is the ability to simulate the loading of an engineering component using numerical methods, including the finite element method (FEM) (25–33). FEA enables obtaining important information about the stress and strain fields in engineering objects for specific loading conditions and fixation. For numerical simulations using FEM, accurate knowledge of the material strength characteristics of the

object under consideration is required (32, 33). As shown in many works, the way of definition of the material model – the true relationship between stresses and strains in many cases determines the correctness of the obtained results of numerical simulations. Utilizing numerical methods for strength analysis allows for both quantitative and qualitative assessments of the current state of the considered object and helps predict its safe operation under specific operating conditions.

Numerous studies in the literature analyze the strength of engineering components and structures using FEM simulations in the literature, covering various applications such as machines and their components, bridges, tanks, and many other objects. For portal cranes, the analysis of standard tests provides a general assessment of the technical condition, typically conducted after a crack or damage has occurred. A more comprehensive evaluation is required for overhead cranes that have been in operation for over 30 years. Chen and He analyzed a portal crane with a rated capacity of 12 tons after more than 50 years of service (34). The numerical model used data from the measurement of the crane's true condition, taking into account any reduction in material thickness. The maximum effective stresses were determined to be about 130 MPa at the location subjected to the highest loads during the crane's operation (34). Similarly, Nemchuk, Nesterov et al. (35, 36) reported comparable findings in their numerical simulations of crane operation. In their work, strain gauge measurements were additionally carried out in the loaded elements, specimens were extracted from the most heavily loaded zones, and strength, ductility and fracture toughness characteristics were determined. The results indicated that while the material properties remained sufficient for failure-free operation, there was a notable decrease in impact resistance in the heavily loaded zones.

This paper focuses on the assessment of the condition of material from a portal crane made of low-carbon steel after long-term service for 33 years based on the results of numerical simulation of the loading of three-point bending (SENB) specimens. True stress-strain relationships for the material were defined based on uniaxial tensile tests of specimens taken from two elements of the portal crane. The paper presents two methods of definition of material dependence consisting of iterative fitting of the best convergence of loading curves of uniaxially tensile specimens and taking

into account the triaxiality and Lode parameters of the material described in papers (37–39). Distributions of mechanical fields and changes in fracture toughness (J -integrals) during simulation loading of specimens were obtained. The results from numerical calculations were compared with experimental results obtained on specimens taken from two crane elements.

MATERIAL AND RESEARCH METHODS

In this study, the condition of material taken from two different elements of a portal crane (Fig. 1a), which was in service for about 33 years, is analyzed. During the long-term operation of the crane, elements A (thickness 16 mm) and B (thickness 12 mm) were cyclically subjected to stresses of different levels. On the basis of numerical calculations, the most loaded elements of the crane were determined, in which the range of stresses, $\Delta\sigma$, was then determined using strain gauge measurements: in element A , the stress range was within 0–130 MPa, while for element B it was 0–55 MPa (3, 40).

The crane was made of low-carbon rolled structural steel. Although the parts are made of the same grade of steel (see Table 1), and both have a ferritic-pearlitic type of microstructure, some differences in their microstructure were observed. For the material of element A , the grains of ferrite and pearlite are larger compared to the steel of element B (see Fig. 1).

EXPERIMENTAL TESTS

In the uniaxial tensile test (41, 42), specimens with a rectangular cross-section of 5.0×3.5 mm and a gauge length of 20.0 mm were tested. A three specimens were tested for each material variant. Dashes were made on the gauge section of the specimens at 2.0 mm intervals. During the tensile test, video recording was used until the specimen failed, allowing strain levels to be determined at each testing point across the entire gauge section and at the most elongated sections, where a local constriction – the neck was formed. The strength and yield characteristics of the tested material are shown in Table 2. Representative nominal (engineering) and true (logarithmic) stress-strain diagrams, $\varepsilon_t - \sigma_t$ are shown in Figure 2. The true values of stress and strain were determined along

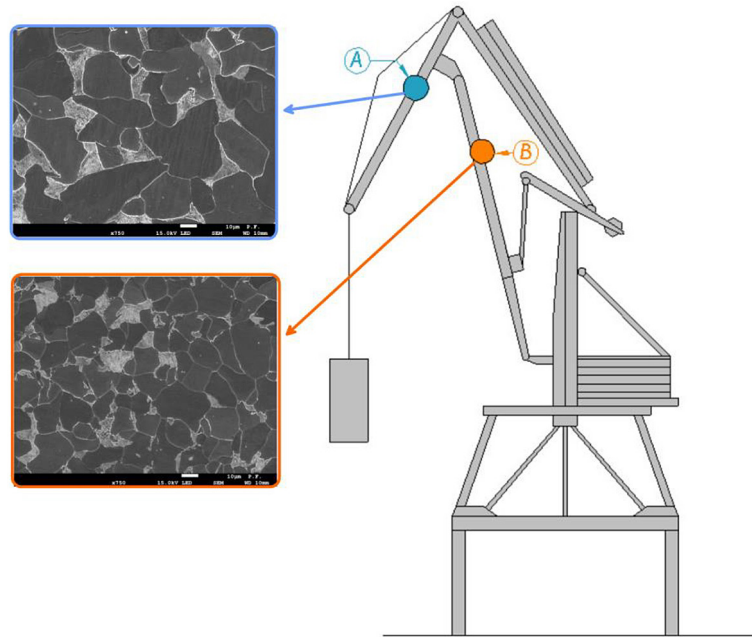


Figure 1. Schematic view of the portal crane under test with microstructure of the different elements of the crane

Table 1. Chemical composition of analyzed steel (% by weight)

C	Si	Mn	Cr	S	P	Cu	Fe
0.17	0.23	0.54	0.11	0.01	0.01	0.1	in balance

the section of uniform specimen elongation according to the formulae:

$$\varepsilon_t = \ln(1 + \varepsilon_{nom}) \quad (1)$$

$$\sigma_t = \sigma_{nom}(1 + \varepsilon_{nom}) \quad (2)$$

where: ε_{nom} – nominal strain; σ_{nom} – nominal stress; ε_t – true strain; σ_t – true stress.

In sections of uniform plastic elongation, the true data were approximated by the Ramberg-Osgood power-law relation (43, 44):

$$\frac{\varepsilon}{\varepsilon_0} = \frac{\sigma}{\sigma_0} + \alpha \left(\frac{\sigma}{\sigma_0} \right)^n \quad (3)$$

where: ε_0 – strain corresponding to yield strength ($\varepsilon_0 = \sigma_0/E$, where E is the Young’s modulus); σ_0 – yield strength of the material; α – constants that depend on the material being considered; n – coefficient (exponent) of material consolidation.

Laboratory tests were carried out to determine the fracture toughness characteristics of the materials analyzed. The fracture toughness was expressed through the values of the J -integral – J_Q . The tests were carried out using the susceptibility change technique, as specified by the

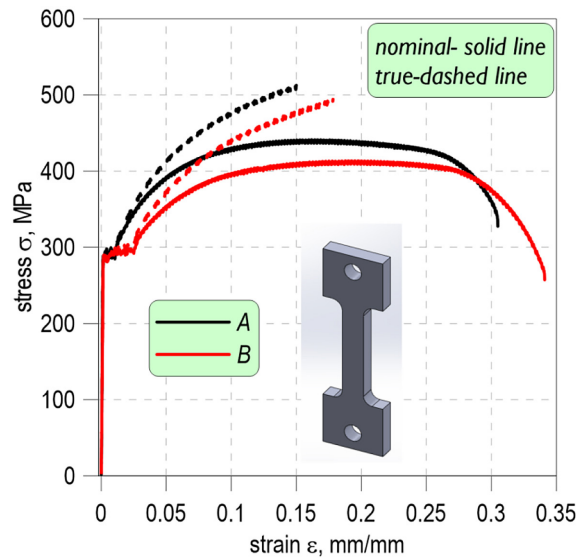


Figure 2. Nominal and true stress-strain relationships of the materials

ASTM standard. Three-point bend specimens of the SENB type, measuring $12 \times 24 \times 96$ mm, were used in the tests. Figure 3 shows the force (F) and deflection (u_{ext}) relationships of the specimens recorded during the laboratory tests. The value of the J -integral was determined at the moment of subcritical crack initiation. The deflection

Table 2. Strength and plasticity characteristics of the materials

Material	E, GPa	$\sigma_{YS,L}$, MPa	$\sigma_{YS,H}$, MPa	σ_{UTS} , MPa	$\sigma_{YS,L}$, MPa	$\sigma_{YS,H}$, MPa	σ_{UTS} , MPa
		Nominal			True		
A	201	284	296	437	287	299	510
B	199	283	299	410	287	302	491

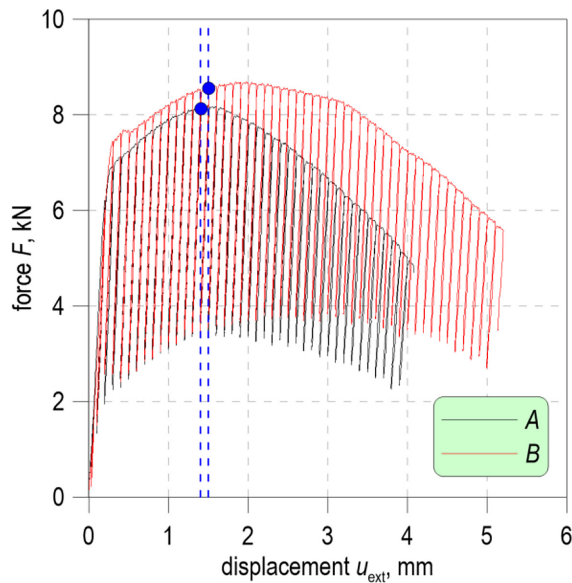


Figure 3. Force-displacement relationships recorded during fracture toughness tests of the specimens

values identified with the moment of crack initiation are shown schematically in Figure 3. The values of the J -integral are summarized in Table 3. The material from the B section of the analyzed port crane was characterized by a higher fracture toughness value. The difference in performance

Table 3. Test critical values fracture toughness results of tested specimens

Material	J_Q , N/mm	u_{ext} , mm
A	123	1.4
B	160	1.5

is about 20%. In this study, the experimentally determined values of the J -integral served as reference values for the results of numerical calculations carried out using the finite element method.

DEFINITION OF THE TRUE STRESS-STRAIN RELATIONSHIP FOR NUMERICAL SIMULATIONS

The proper definition of the material model, i.e. the true stress-strain relationship, is very important for its usage in numerical simulations. A definition of the material description in two ranges is required: linear-elastic and plastic. In the elastic range, two elastic constants are used for definition: Young’s modulus and Poisson’s ratio. The occurrence of plastic strain in the material under load makes it necessary to define the

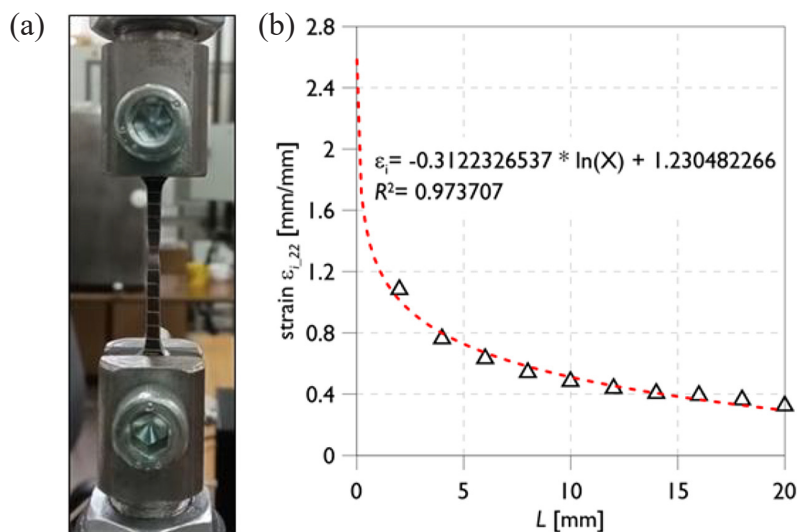


Figure 4. Determination of true strain levels in the material: (a) view of a uniaxially tensile specimen with gauge sections; (b) extrapolation of the trend line to the grain size of the material microstructure

plastic part of the material. In the first instance, an important step is to determine the critical true strain and stress levels in the material. In the next step, a calibration method must be chosen that allows the force-displacement curves obtained in laboratory tests and those determined numerically to converge. The critical true strain of the material, $\varepsilon_{c,t}$, was determined by measuring the elongation of the sections on the specimen (view of specimen with sections see Fig. 4a). For this purpose, an approach based on the extrapolation of a trend line (45) was used, which describes the dependence of the strain change determined on increasingly smaller increments, $\Delta_i = L_i - L_{0i}$, of the measuring sections, L_{0i} , on an amount equal to the material grain diameter, d (example see Fig. 4b):

$$\varepsilon_{c,t} = \lim_{L_{0i} \rightarrow d} \frac{L_i - L_{0i}}{L_{0i}} \quad (4)$$

Subsequently, the modelling of the true stress-strain relationship, knowledge of which is necessary to perform numerical calculations in terms of plastic deformation of the material, was carried out. For this purpose, two approaches were used: (i) modelling according to the procedure proposed by Bai-Wierzbicki with modifications by Neimitz (BWN) (37–39) and (ii) modelling based on an iterative determination (IM) of the material relationship by best fitting the experimental and numerically calculated specimen loading relationship, $F-u$ (46–48). In the iterative approach, the true stress-strain relationship is initially estimated based on a power-law range of points from yield stress to the true critical stress ($\sigma_{c,t}$) and strain ($\varepsilon_{c,t}$) values. The true critical stress level was obtained by relating the force at rupture to the true area of the specimen after testing. The determination of the critical strain ($\varepsilon_{c,t}$) values is shown in Figure 4, and it may be noted that other methods of estimating the critical stress ($\sigma_{c,t}$) and strain ($\varepsilon_{c,t}$) values are presented in the papers (5, 45).

The Bai-Wierzbicki procedure considers the influence of the stress triaxiality factor η and the Lode parameter L . The relationship determining the plasticization stresses (equation 5) is used as a basis:

$$\sigma_{yld} = \bar{\sigma}(\bar{\varepsilon}_{pl}) [1 - c_\eta(\eta - \eta_0)] \cdot \left[c_\theta^s + (c_\theta^{ax} - c_\theta^s) \left(\gamma - \frac{\gamma^{m+1}}{m+1} \right) \right] \quad (5)$$

In equation (5), $\bar{\sigma}(\bar{\varepsilon}_{pl})$ is a function describing true stresses with respect to plastic strain (obtained from experimental studies). The quantity η is the stress triaxiality factor:

$$\eta = \frac{\sigma_m}{\sigma_{eff}} \quad (6)$$

where: σ_m – medium stresses; σ_{eff} – effective stresses, η_0 – reference stress triaxiality factor (for a smooth specimen, uniaxially tensioned – $\eta_0 = 0.33$).

The γ function takes values within the limits 0–1, with 0 occurring for the cases of plane strain and shear and 1 for axial symmetry. The γ function is calculated from the relationship:

$$\begin{aligned} \gamma &= \frac{\cos\left(\frac{\pi}{6}\right)}{1 - \cos\left(\frac{\pi}{6}\right)} \left[\frac{1}{\cos\left(\theta - \frac{\pi}{6}\right)} - 1 \right] = \\ &= 6,46 \left[\sec\left(\theta - \frac{\pi}{6}\right) - 1 \right] \end{aligned} \quad (7)$$

where: θ – lode angle, taking a value in the $0 \leq \theta \leq \pi/3$ range.

The lode angle is a function of the second and third invariants of the stress deviator:

$$\cos(3\theta) = \left(\frac{r}{\sigma_{eff}} \right)^3 = \xi = \frac{27 J_3}{2 \sigma_{eff}^3} \quad (8)$$

$$\begin{aligned} r &= \left[\frac{27}{2} \det(s_{ij}) \right]^{\frac{1}{3}} = \\ &= \left[\frac{27}{2} (\sigma_{11} - \sigma_m)(\sigma_{22} - \sigma_m)(\sigma_{33} - \sigma_m) \right]^{\frac{1}{3}} \end{aligned} \quad (9)$$

The procedure also uses a normalized Lode angle, $\bar{\theta}$. It takes values in the range from -1 to 1, described by the relation:

$$\bar{\theta} = 1 - \frac{6\theta}{\pi} = 1 - \frac{2}{\pi} \arccos \xi \quad (10)$$

The magnitude of the Lode parameter, L , can be represented by principal stress components in the form:

$$L = - \frac{2\sigma_{II} - \sigma_I - \sigma_{III}}{\sigma_I - \sigma_{III}} \quad (11)$$

where: σ_I – the highest component of the principal stress, while σ_{III} the smallest.

There is a relationship between the quantities ξ and L :

$$\xi = L \frac{9 - L^2}{\sqrt{(L^2 + 3)^3}} \quad (12)$$

The quantities c_η , c_θ^t , c_θ^c , c_θ^s and m are determined experimentally. In equation 5, the magnitude of c_θ^{ax} depending on the value of the Lode angle, $\bar{\theta}$ is: $c_\theta^{ax} = c_\theta^t$ for $\bar{\theta} \geq 0$, $c_\theta^{ax} = c_\theta^c$ for $\bar{\theta} \leq 0$. For the stress-strain curve obtained experimentally in the tensile test: $c_\theta^t = 1$, in the compression test: $c_\theta^c = 1$, and in the torsion test: $c_\theta^s = 1$. A member with the value m was added to the formula for the yield function so that the yield surface is smooth and differentiable with respect to the Lode angle ($\gamma = 1$). The parameter m usually takes values around unity.

In the work of Neimitz and co-workers (39, 49), it was proposed that the stress triaxiality parameter η should be calculated as the average value after the smallest cross-section of the analyzed specimen in each calculation step. In the smallest section, there were maximum stress levels, triaxiality and strain. It was assumed that the parameter η varies linearly from the initial value η_i to the value at failure η_f . The relationship between the stress triaxiality factor η and the strains at each calculation step was determined. The resulting points were approximated by a linear function and used in the calibration procedure. Similarly, the distributions of the Lode parameter were determined.

In addition, a formula has been implemented that allows very accurate calibration of the tensile curve at this loading stage, considering the effect of material softening. This phenomenon is identified with the initiation, development and coalescence of voids in the material before the moment of destruction. A formula has been proposed to calculate the magnitude of c'_η in the form (39):

$$c'_\eta = c_\eta [1 + H(\varepsilon_{pl,0})(\varepsilon_{pl} - \varepsilon_{pl,0})]^\zeta \quad (13)$$

where: $\varepsilon_{pl,0}$ – the amount of plastic strain from the level at which the softening effect on

the tensile curve occurs (equated with the moment of void growth); $H(\varepsilon_{pl,0})$ – Heaviside's function.

The numerical model and loading scheme for the tensile specimen are shown in Figure 5a. The three-dimensional model of the tensile specimen was developed with Abaqus ver. 6.12 (50). The dimensions of the numerical specimen model were the same as the geometry of the specimens used in the uniaxial tensile tests. For symmetry reasons, 1/8 of the specimen was modelled. This reduced the number of nodes in the model and the calculation time. The front of the crack tip was modelled as an arc with a radius of 12 μm . The specimen model contained 2920 nodes, and 8-node, three-dimensional finite elements were used. The size of the finite elements was reduced, approaching the symmetry planes of the specimen so that the dimension of the smallest element was 0.05 mm in this area. The developed finite element mesh was verified with a dedicated tool in Abaqus, and no elements of unacceptable quality were detected. The boundary conditions assumed: on the wall, perpendicular to the Y axis, displacements in the Y direction and rotation in the X and Z directions were blocked; on the wall perpendicular to the X axis, the possibilities of displacements in the X direction and rotation in the Y and Z directions were blocked; on the wall along the Z axis, displacements in the Z direction and rotation in the X and Y directions were blocked. The numerical model of the tensile specimen assumed a force in the form of a displacement applied to the wall according to the scheme in Figure 5a. The displacement value was determined from data recorded during uniaxial tensile tests in the laboratory.

Figure 6 shows the plots of the $F-u$ relationship for specimens A and B subjected to experimental tests and the values obtained by numerical

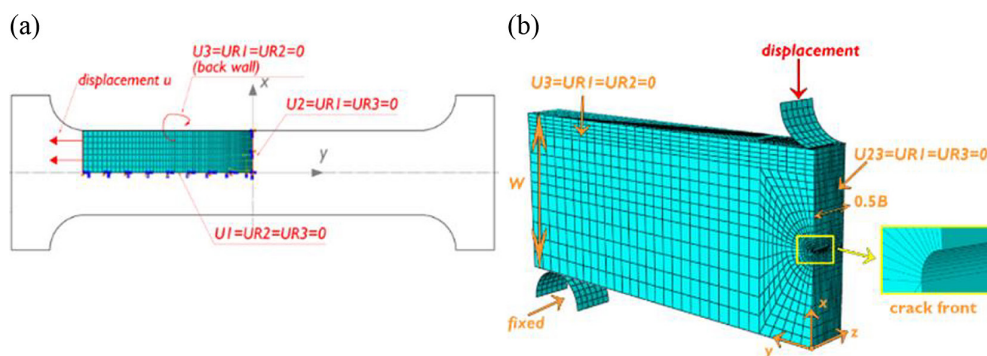


Figure 5. Numerical model and loading scheme for: (a) tensile specimen, (b) SENB specimen

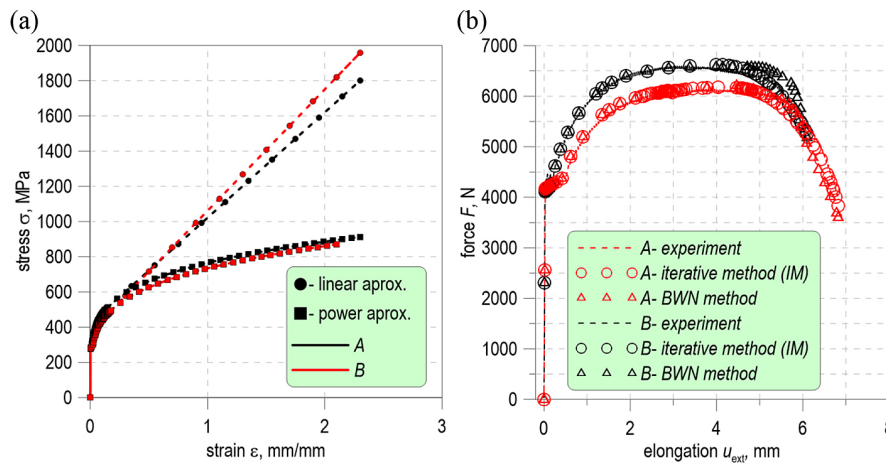


Figure 6. Results obtained from the true material models are as follows: (a) stress-strain relationships used in the numerical calculations; (b) experimental and numerical $F-u$ curves

calculations, using the material relationships obtained by applying the two methods analyzed (Fig. 6a: BWN and IM). The criterion for accuracy was the best possible convergence of the force-elongation relationship ($F-u$) recorded during the experimental tests and that obtained from the numerical calculations. Good convergence of experimental and computational data was obtained for both the IM and the BWN procedures. This demonstrates the correctness of the defined material constitutive relations: $\sigma_i = f(\epsilon_i)$. These material relations were used in the following studies when simulating the loading of SENB specimens.

NUMERICAL MODELLING AND LOAD SIMULATION OF SENB SPECIMENS

The stress and strain fields in the area before the crack tip determine the subsequent crack development mechanism, which is ductile or brittle. The occurrence of higher levels of stress components σ_{ij} in front of the crack tip, in particular the component normal to the crack plane σ_{22} , and the stress triaxiality factor η indicates a higher propensity of the material to realize cleavage fracture and lower fracture toughness (51). The criterion formulated by Rice, Knott, and Ritchie (RKR) (52) postulated that brittle fracture would be realized when the stress level σ_{22} exceeds a critical value over a certain interval (52, 53) or area (51). Later studies (51) showed that the level of stress triaxiality factor η and effective plastic strain $\epsilon_{pl,eff}$ also affect the nature of the development of the fracture process in the material. Brittle fracture is

realised when high values of stress σ_{22} and stress triaxiality factor η are reached at negligible levels of plastic strain $\epsilon_{pl,eff}$. On the other hand, at high levels of $\epsilon_{pl,eff}$ and moderate values of η , ductile fracture occurs through the development of voids. Shear fracture development is expected at high values of $\epsilon_{pl,eff}$ and low values of η (39).

Modelling and load simulations of the SENB specimens were carried out to assess the fracture toughness of test materials A and B. The numerical model of the SENB specimen is shown in Figure 5b. Due to the existing symmetry, the model assumed the development of $1/4$ of the SENB specimen. The top and bottom rollers were modelled as a shell object. The numerical model of the specimen was divided into 21 layers in the thickness direction. 8-node and three-dimensional finite elements were used. The size of the elements was reduced as the crack front area was approached (the smallest finite element size was 65 μm). The SENB specimen model included 20680 nodes. The choice of finite element size and the way the specimen was partitioned into layers was preceded by preliminary analyses in order to achieve convergence of the results obtained. The crack front was modelled as an arc with a radius of 12 μm . In the definition of the boundary conditions, the following was assumed: the possibility of displacement of the cracked part of the specimen (XOZ direction according to the reference system on the fig. 5b) was restrained, the possibility of displacement of the un-cracked part of the XOZ specimen in the Y direction was blocked, the possibility of displacement of the mid-plane of the specimen (XOY direction according to the

reference system on the Fig. 5b) in the Z direction was blocked, and the lower rollers was completely immobilized. In the load simulation, the displacement of the upper roller pressing on the specimen was set. The material of the specimens was defined according to the constitutive relations described in the previous chapter. The specimens were loaded with the displacement of the roller in the X direction, which corresponded to the realization of a three-point bending scheme.

The true stress-strain relationships obtained by applying different procedures for their definition (the IM and the BWN) were implemented

into the numerical model of the SENB specimen. The distributions of stress components σ_{11} , σ_{22} , and σ_{33} (Fig. 7), the stress triaxiality factor η (Fig. 8a) and the effective plastic strain (Fig. 8b) were determined taking into account the considered relations (in the graphs l is the distance from the crack front). Figures 7 and 8 show the results of numerical calculations for the two displacement values used in the simulations: 1.0 and 1.2 mm. The results obtained are summarized in Table 4. No significant differences were observed in the distributions of the stress components σ_{11} and σ_{33} for the two different methods of defining the

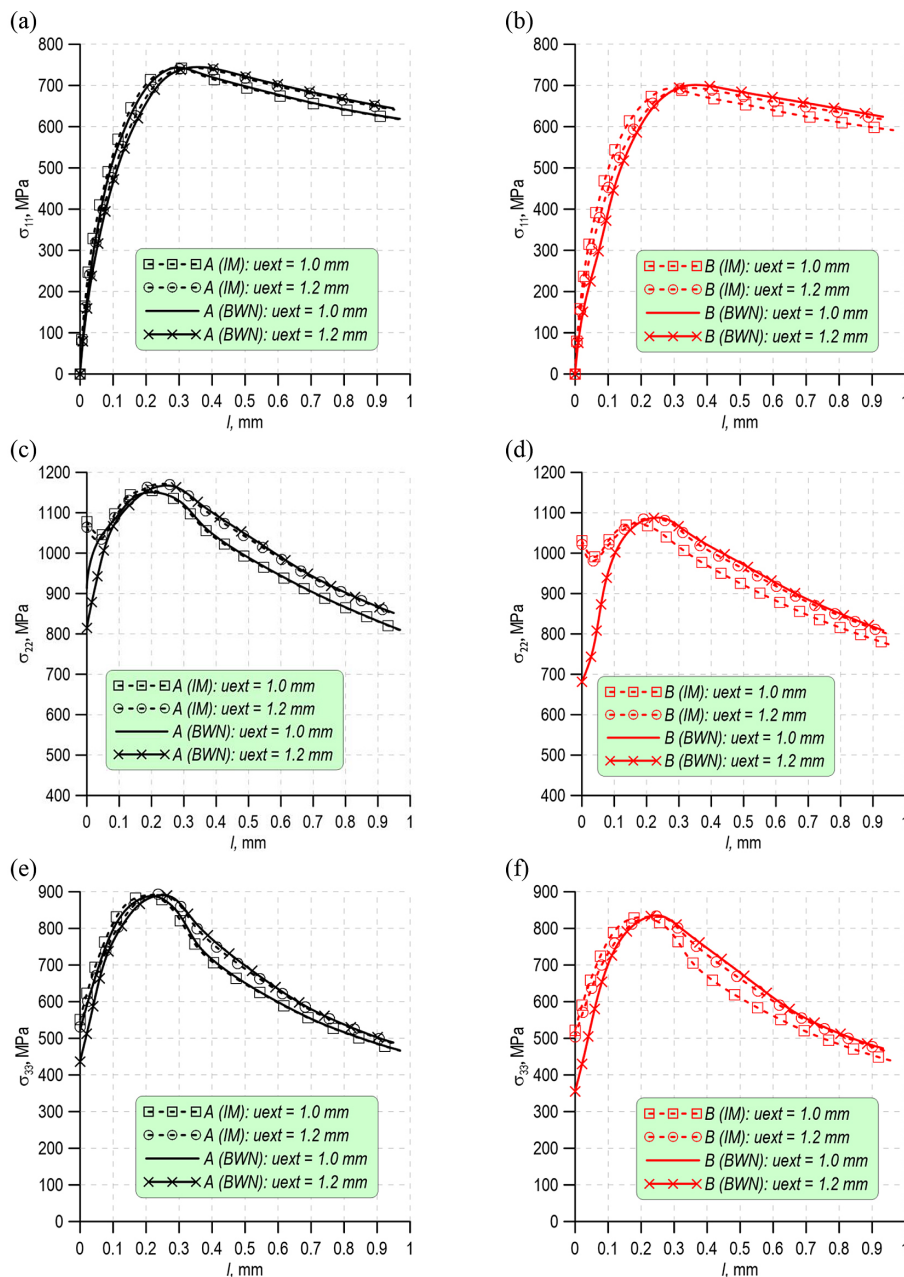


Figure 7. Numerically determined stress distributions for material A: (a) σ_{11} ; (c) σ_{22} ; (e) σ_{33} ; and material B: (b) σ_{11} ; (d) σ_{22} ; (f) σ_{33}

material dependence. Differences were observed for the component σ_{22} . When the true stress-strain relationship determined according to the IM was used in the numerical calculations in the immediate vicinity of the crack tip, an increase in stress σ_{22} was observed (Fig. 7c, 7d). This trend in the behavior of the σ_{22} component occurred for all materials: *A* and *B*. The differences were small for the opening stress maxima σ_{22} ; when defining the material model using the IM, the maximum occurred at a slightly further distance from the crack front. The different methods of determining the σ_t - ε_t relationship of the material used in the numerical calculations of notched specimens showed no significant effect on the distributions of the stress triaxiality factor and the effective plastic strain.

Higher values of the normal components of the stress tensor occurred for material *A*. In the case of opening stress σ_{22} , the difference between the maximum values was about 7%. For material *A*, the locations of the σ_{22} stress maxima were closer to the crack front with respect to material *B* (Fig. 7c, 7d).

The analyzed specimens were characterized by relatively high levels of effective plastic strain, in the range of 100–140%. Higher levels of strain are found in the material *B*. The stress triaxiality factor showed similar values for the studied steels, with a tendency to be some higher for material *B*. As the numerically simulated deflection values of the SENB specimens increased, 1.0 mm and 1.2 mm, the maximum values of the η coefficient decreased. The location of the maximum value was moving away from the crack front.

From the presented distributions: stress components, strains and stress triaxiality factor, it can be concluded that material *A* is more prone to fracture than *B*.

Numerical simulations of the loading of the SENB specimen were carried out for deflection values corresponding to the subcritical crack initiation moment. This moment was determined by fracture toughness tests using the compliance change method. The crack initiation moment was determined to be critical. As indicated in Figure 3 and Table 3, the deflections of the specimens at the critical moment were: for *A* – 1.4 mm and for *B* – 1.5 mm. For the above-mentioned values of deflections in the SENB specimens, the distributions of the opening stress and stress in front of the crack front were determined. The values of the *J*-integral were also determined and confronted with the results of J_Q obtained during laboratory tests. Specimen *B* showed lower levels of opening stress σ_{22} compared to specimen *A* (Fig. 9a). The difference in the maximum values of stress σ_{22} was within 7%. The values of the *J*-integral determined numerically were compared with the results of laboratory tests on fracture toughness – the critical values J_Q . A good agreement between experimental and numerical results was obtained. The largest difference occurred for calculations at the critical moment (Fig. 9b); for specimen *B*, it was about 8% and about 3% for specimen *A*. This may be due to the consequence of the larger deflection value assumed in the numerical simulation of loading specimen SENB, resulting in significant deformation of the finite element mesh in the model.

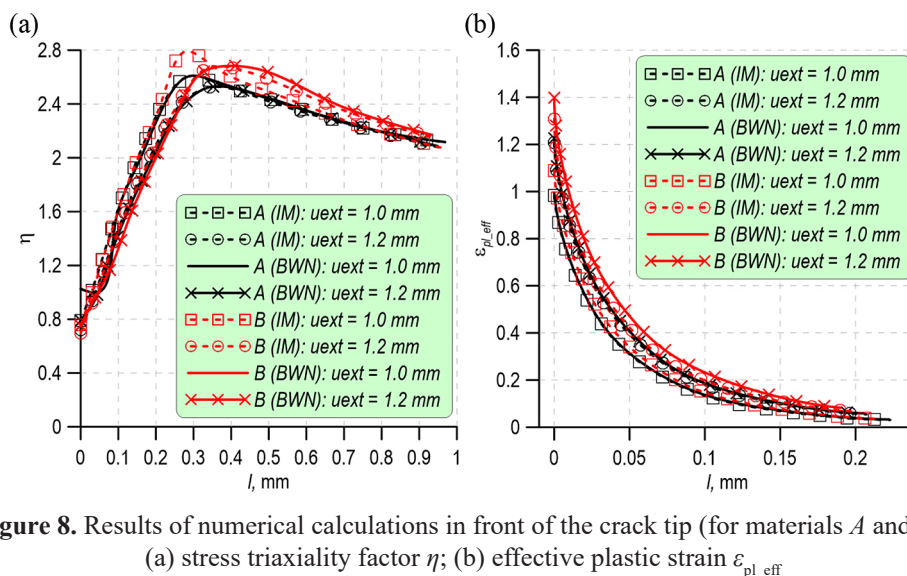


Figure 8. Results of numerical calculations in front of the crack tip (for materials *A* and *B*): (a) stress triaxiality factor η ; (b) effective plastic strain ε_{pl_eff}

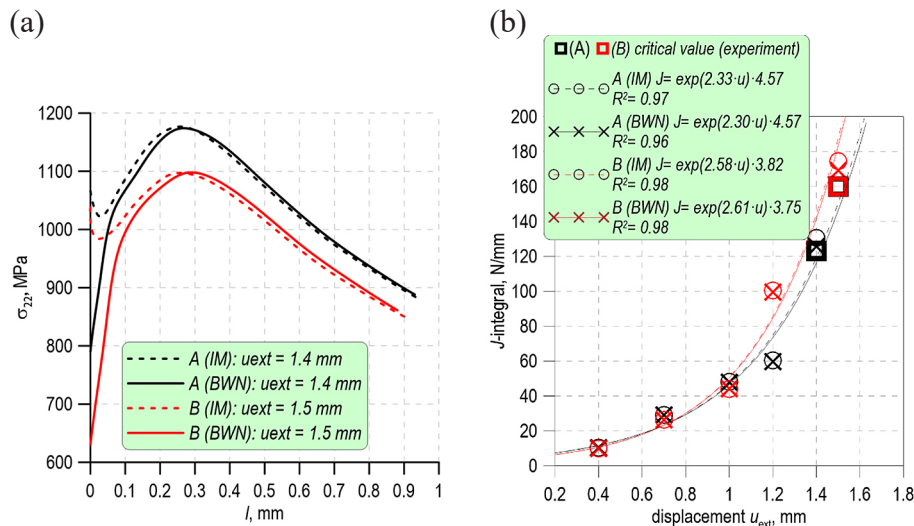


Figure 9. Results of numerical simulations for the subcritical fracture initiation moment distributions: (a) of the opening stress σ_{22} ; (b) of the J -integral

The higher values of the numerical calculated J -integral were obtained for specimens designated B . The higher level of the J -integral at the same deflection in specimen B indicates the need for a higher level of cumulative energy compared to specimens with lower values of the J -integral. This, therefore, means that material B is more resistant to fracture than the other material considered. However, the results of the numerical simulations only allow a qualitative comparison of the materials investigated. The results of numerical calculations for the maximum values of the stress component distributions, stress triaxiality factor and effective plastic strain, are presented in Table 4. The calculations were performed for two methods of defining the material true stress-strain relationship for BWN and IM.

DISCUSSION

This paper presents an assessment of the structural integrity of material from portal crane components using the numerical finite element calculation method. Developments in computer techniques and numerical calculation software allow accurate assessment of material condition (22, 54). The proposed method is based on the implementation of a tensile test carried out experimentally. A crucial aspect of these methods is the correct definition of the material model – the relationship between true strains and stresses, $\sigma_t - \varepsilon_t$. Various methods are proposed in the literature to determine this relation (38, 45, 46, 48, 55). As a verification of the validity of the relationship σ_t

Table 4. Summary of the numerical calculation results obtained

Mat.	u_{ext} , mm	σ_{11} max	l	σ_{22} max	l	σ_{33} max	l	η max	l	$\varepsilon_{pl,eff}$ max	l	
		MPa		mm		MPa		mm		MPa		mm
A	BWN	1.00	743.14	0.29	1149.34	0.22	888.29	0.22	2.61	0.29	0.99	1.00
		1.20	743.81	0.34	1164.76	0.27	887.97	0.27	2.52	0.34	1.23	1.00
		1.40	739.13	0.47	1173.15	0.25	882.26	0.25	2.45	0.47	1.43	1.00
	IM	1.00	743.18	0.29	1152.48	0.16	888.50	0.22	2.61	0.29	0.98	1.00
		1.20	742.92	0.34	1169.20	0.21	889.39	0.21	2.52	0.34	1.21	1.00
		1.40	736.64	0.32	1176.81	0.26	887.24	0.26	2.43	0.48	1.41	1.00
B	BWN	1.00	689.74	0.28	1068.18	0.21	825.53	0.21	2.72	0.35	1.12	1.00
		1.20	696.67	0.32	1085.86	0.26	835.02	0.26	2.66	0.48	1.40	1.00
		1.50	694.40	0.62	1097.06	0.27	817.75	0.27	2.58	0.62	1.67	1.00
	IM	1.00	692.62	0.28	1072.63	0.15	829.27	0.22	2.79	0.28	1.09	1.00
		1.20	693.18	0.33	1085.95	0.20	830.53	0.27	2.66	0.33	1.31	1.00
		1.50	688.02	0.45	1096.04	0.24	816.47	0.24	2.51	0.65	1.71	1.00

– ε_t , it is assumed to check the convergence of the specimen load charts during the tensile test determined experimentally and numerically. It was proposed two methods of the definition of the dependency $\sigma_t - \varepsilon_t$ – the iterative selection of the relation and its development based on the model proposed in papers by Bai, Wierzbicki and Neimitz (39, 56). Applying both $\sigma_t - \varepsilon_t$ relations developed from these approaches in numerical calculations indicated good agreement between experimental and numerical graphs of uniaxially loading specimens.

These relationships $\sigma_t - \varepsilon_t$ were used when simulating loading specimens containing a crack (SENB). Similar and close stress and strain distributions in front of the crack tip were obtained during calculating using both $\sigma_t - \varepsilon_t$ relationships. The distributions of the σ_{11} and σ_{33} components are similar in the wide region before the crack tip. Only in the distributions of σ_{22} , immediately in front of the crack tip, were some differences observed. In the σ_{22} stress distributions, calculated using true stress-strain relations defined by IM, the data increases before the top of the crack. It is no right trend, as they should decrease. The reason may be that the softening of the material due to the growth of voids in the immediate vicinity in front of the crack tip is not taken into account. This effect is considered in the BWN model through the function proposed by Neimitz (39, 49).

The results presented here allow us to conclude that a comparative assessment of the material condition can be performed using both methods to define the relationship $\sigma_t - \varepsilon_t$; because the plot of stress is similar on most of the range and, most importantly, at maximum values. However, the BWN method to define the relationship $\sigma_t - \varepsilon_t$, although requiring a greater effort in definition, allows obtaining physically correct stress distributions even in the immediate vicinity before the crack tip. Higher values in the distributions of the various stress components were recorded in material *A* compared to *B*, indicating that *A* is more susceptible to fracture. In contrast, specimens from material *B* are characterized by higher levels of plastic strain.

An important step in the presented research is to determine the value of the *J*-integral characterizing the material from numerical simulation of specimen loading. The paper shows that relatively good agreement was achieved between the *J*-integral results from laboratory tests and numerical simulations.

The presented approach allows an assessment of the fracture toughness of the material, with knowledge only of the true stress-strain relationship in cases where suitable test specimens (e.g. three-point bending SENB specimens) cannot be taken from the engineering component under analysis. On the basis of the numerical simulation of the loaded material, it is possible to determine a number of characteristic quantities in the material that allow a correct qualitative assessment of its fracture toughness state.

CONCLUSIONS

The current condition of portal crane elements was assessed using numerical simulation using the finite element method of the load of three-point bending specimens and true stress-strain relationships $\sigma_t - \varepsilon_t$. The constitutive dependencies $\sigma_t - \varepsilon_t$ of the material from different crane elements were defined based on the uniaxial tensile test data using two methods – the iterative fitting method of the experimental and numerical relationship and the method considering the stress triaxiality and the Lode parameter. The accuracy of the defined stress-strain relationships was verified by comparing the force-elongation graphs determined experimentally and numerically. For the investigated steel elements, similar stress and strain distributions in front of the crack tip were obtained by calculating using both $\sigma_t - \varepsilon_t$ relationships. Some differences in the distributions of σ_{22} , immediately in front of the crack tip, were only observed. The distributions of the σ_{11} and σ_{33} components are similar in the wide region before the crack tip. Only in the distributions of σ_{22} , immediately in front of the crack tip, were some differences observed. Corresponding to this analysis result, a comparative assessment of the material condition can be performed using both methods to define the relationship $\sigma_t - \varepsilon_t$. However, an insignificant increase in the values before the crack tip for the σ_{22} stress distributions calculated using true stress-strain relations defined by the iterative fitting method was observed. This result can be associated with the material softening due to the void growth in the immediate vicinity in front of the crack tip, which is not considered in this case. At the same time, the method considering the stress triaxiality and the Lode parameter to define the relationship $\sigma_t - \varepsilon_t$ allows obtaining physically correct stress distributions even in the immediate

vicinity before the crack tip despite requiring a greater effort in the definition.

The presented approach enables an assessment of the material's fracture toughness using only the true stress-strain relationship and numerical simulation of specimen loading. The trends in the stress component distributions indicate a high level of fracture toughness of the tested materials, ensuring a ductile nature of subcritical crack growth. A relatively good correlation between the J-integral values obtained by both experimentally and numerical simulations was revealed. Therefore, the approach can be used for evaluating the fracture toughness of the material in cases where suitable test specimens (e.g. three-point bending SENB specimens) cannot be extracted from the engineering component for in-laboratory testing.

This APC project was financed by the Minister of Science of Poland, Grant numbers 01.0.13.00/1.02.001/SUBB.MKKM.25.001.

REFERENCES

1. Lesiuk G, Szata M, Bocian M. The mechanical properties and the microstructural degradation effect in an old low carbon steels after 100-years operating time. *Archives of Civil and Mechanical Engineering*. 2015; 15(4).
2. Lepretre E, Chataigner S, Dieng L, Gaillet L, Canard H. Numerical and experimental investigations of hot driven riveting process on old metal structures. *Engineering Structures*. 2016; 127: 583–93.
3. Pustovyi VM, Semenov PO, Nemchuk OO, Hredil MI, Nesterov OA, Strelbitskyi VV. Degradation of steels of the reloading equipment operating beyond its designed service Life. *Mater Sci*. 2022; 57(5): 640–8.
4. Nykyforchyn HM, Tsyruł'nyk OT. Specific features of the in-service bulk degradation of structural steels under the action of corrosive media. *Strength Mater*. 2009; 41(6): 651–63.
5. Zvirko O, Tsyrułnyk O, Lipiec S, Dzioba I. Evaluation of corrosion, mechanical properties and hydrogen embrittlement of casing pipe steels with different microstructure. *Materials*. 2021; 14(24): 1–17.
6. Dobrzański J, Hernas A, Moskal G. Microstructural degradation in boiler steels: materials developments, properties and assessment. W: Oakey JE, redaktor. *Power Plant Life Management and Performance Improvement*. Woodhead Publishing; 2011. 222–71. (Woodhead Publishing Series in Energy).
7. Zieliński A, Dobrzański J, Purzyńska H, Golański G. Changes in properties and microstructure of high-chromium 9–12%Cr steels due to long-term exposure at elevated temperature. *Archives of Metallurgy and Materials*. 2016.
8. Major Z, Bodnár L, Merczel DB, Szép J, Lublój É. Analysis of the heating of steel structures during fire load. *Emerging Science Journal*. 2024; 8(1): 1–16.
9. Koo KY, Brownjohn JMW, List DI, Cole R. Structural health monitoring of the Tamar suspension bridge. *Structural Control and Health Monitoring*. 2013; 20(4): 609–25.
10. Kulka J, Mantic M, Fedorko G, Molnar V. Analysis of crane track degradation due to operation. *Engineering Failure Analysis*. 2016; 59: 384–95.
11. Hredil M, Krechkovska H, Student O, Tsyrułnyk O. Brittle fracture manifestation in gas pipeline steels after long-term operation. *Procedia Structural Integrity*. 2020; 28: 1204–11.
12. Kossakowski PG. Mechanical properties of bridge steel from the late 19th century. *Applied Sciences*. 2021; 11(2): 478.
13. Hrabovskyy R, Kryzhanivskyy Y, Tuts O, Mandruk O, Tyrlych V, Artym V, i in. Impact of long-term operation on reliability and durability of natural gas pipeline: Potential environmental consequences of accidents. *Procedia Structural Integrity*. 2024; 59: 112–9.
14. Krechkovska HV, Voitovich AA, Dzyubyk AR, Kindratskyi BI, Lampitskyi OS, Bohun LI. Differences in structure and properties of the beam metal of the bridge structure. *Mater Sci*. 2024; 59(6): 720–6.
15. Adamczak-Bugno A, Krampikowska A. The acoustic emission method implementation proposition to confirm the presence and assessment of reinforcement quality and strength of fiber–cement composites. *Materials*. 2020; 13(13): 2966.
16. Grajčevci F, Mujaj A, Kryeziu D, Rudhani G, Shkodrani N. Experimental and numerical research on the behavior of steel columns with circular hollow cross sections. *Civil Engineering Journal*. 2024; 10(5): 1577–88.
17. Putra WT, Setiawan AF, Saputra A, Satyarno I, Pratama HY. Frictional axial resistance of clamped split pocket mechanism steel structural joint: An experimental study. *Civil Engineering Journal*. 2024; 10(9): 2870–87.
18. James Raj JRD, Raja V, Srikanth D, Surendran H, Nickolas MM. Non-destructive testing (NDT) techniques for low carbon steel welded joints: A review and experimental study. *Materials Today: Proceedings*. 2021; 44.
19. Khedmatgozar Dolati SS, Caluk N, Mehrabi A, Khedmatgozar Dolati SS. Non-destructive testing applications for steel bridges. *Applied Sciences*. 2021; 11: 9757.
20. Zhou P, Zhou G, Zhu Z, He Z, Ding X, Tang C. A review of non-destructive damage detection methods for steel wire ropes. *Applied Sciences*. 2019; 9: 2771.

21. Świt G, Dzioba I, Ulewicz M, Lipiec S, Adamczak-Bugno A, Krampikowska A. Experimental-numerical analysis of the fracture process in smooth and notched V specimens. *Production Engineering Archives*. 2023; 29(4): 444–51.
22. Adamczak-Bugno A, Lipiec S, Vavruš M, Koteš P. Non-destructive methods and numerical analysis used for monitoring and analysis of fibre concrete deformations. *Materials*. 2022; 15(20): 7268.
23. Kubit A, Macek W, Zielecki W, Szawara P, Kłonica M. Fracture surface topography parameters for S235JR steel adhesive joints after fatigue shear testing. *Adv Sci Technol Res J*. 2023; 17(5): 130–9.
24. Kurpanik K, Sławski S, Machoczek T, Woźniak A, Duda S, Kciuk S. Assessment of the conveyor belt strength decrease due to the long term exploitation in harmful conditions. *Adv Sci Technol Res J*. 1 sierpień 2024; 18(4): 1–11.
25. Dubyk Y, Seliverstova I, Bogdan A. Stress assessment of single mitered bend using approximate cylindrical shell solutions. *Procedia Structural Integrity*. 2019; 18: 630–8.
26. Birnbaum P, Meza-García E, Landgraf P, Grund T, Lampke T, Kräusel V. Experimental and numerical assessment of the hot sheet formability of martensitic stainless steels. *Journal of Manufacturing and Materials Processing*. 2020; 4(4): 122.
27. Tang L, Ince A, Zheng J. Numerical modeling of residual stresses and fatigue damage assessment of ultrasonic impact treated 304L stainless steel welded joints. *Engineering Failure Analysis*. 2020; 108: 104277.
28. Yang F, Veljkovic M, Liu Y. Ductile damage model calibration for high-strength structural steels. *Construction and Building Materials*. 10 grudzień 2020; 263: 120632.
29. Asadipoor M, Kadkhodapour J, Pourkamali Anaraki A, Sharifi SMH, Darabi ACh, Barnoush A. Experimental and numerical investigation of hydrogen embrittlement effect on microdamage evolution of advanced high-strength dual-phase steel. *Met Mater Int*. 2021; 27(7): 2276–91.
30. Wciślik W, Lipiec S. Voids Development in metals: Numerical modelling. *Materials*. 2023; 16(14): 4998.
31. Ivanytskyi YaL, Blikharskyi ZYa, Maksymenko OP, Panchenko OV, Blikharskyi YaZ. Development of the methodology for monitoring the technical state of bridge structures and establishment of safe operating period. *Mater Sci*. 2024; 59(6): 711–9.
32. Lipiec S, Pała R, Dzioba I. Experimental-numerical analysis of the fracture process of Al-Al-Ti laminated composite. *Engineering Failure Analysis*. 2022; 141: 106715.
33. Zvirko OI, Lipiec S, Vengreniuk OI, Dzioba I. Evaluation of the stress-strain state at the crack tip in casing pipes based on numerical simulation. *Mater Sci*. 2023; 58(4): 460–5.
34. Chen M, He S. Structural Strength Analysis and Stress Testing of Portal Crane based on Finite Element Method. *J Phys: Conf Ser*. 2022; 2366(1): 012003.
35. Nemchuk OO, Nesterov OA. In-service brittle fracture resistance degradation of steel in a ship-to-shore portal crane. *Strength Mater*. 1 marzec 2020; 52(2): 275–80.
36. Nemchuk O, Hredil M, Pustovoy V, Nesterov O. Role of in-service conditions in operational degradation of mechanical properties of portal cranes steel. *Procedia Structural Integrity*. 2019; 16: 245–51.
37. Wierzbicki T, Bao Y, Lee YW, Bai Y. Calibration and evaluation of seven fracture models. *International Journal of Mechanical Sciences*. 2005; 47(4): 719–43.
38. Bai Y, Wierzbicki T. A new model of metal plasticity and fracture with pressure and Lode dependence. *International Journal of Plasticity*. 2008; 24(6): 1071–96.
39. Neimitz A, Galkiewicz J, Lipiec S, Dzioba I. Estimation of the onset of crack growth in ductile materials. *Materials*. październik 2018; 11(10): 2026.
40. Zvirko O, Dzioba I, Hredil M, Pała R, Oliynyk O, Furmańczyk P. Specimen size effect on the tensile properties of rolled steel of long-term-operated portal crane. *Materials*. styczeń 2023; 16(8): 3017.
41. ASTM E8 / E8M-16ae1. ASTM E8 / E8M-16ae1, Standard Test Methods for Tension Testing of Metallic Materials [Internet]. West Conshohocken: ASTM International; 2016. Dostępne na: www.astm.org
42. PN-EN ISO 6892-1:2020-05. PN-EN ISO 6892-1:2020-05, Metallic materials — Tensile testing — Part 1: Method of test at room temperature [Internet]. Geneva: International Organization for Standardization; 2019. Dostępne na: www.astm.org
43. Anderson TL. *Fracture Mechanics. Fundamentals and Applications*. Third Edition. Taylor and Francis Group; 2005.
44. Ramberg W, Osgood WR. Description of stress-strain curves by three parameters [Internet]. 1943. Dostępne na: <https://ntrs.nasa.gov/citations/19930081614>
45. Dzioba I, Lipiec S, Pała R, Furmańczyk P. On characteristics of ferritic steel determined during the uniaxial tensile test. *Materials*. 2021; 14(11): 1–17.
46. Depreński Ł, Seweryn A. Ductile fracture of notched aluminum alloy specimens under elevated temperature part 2– Numerical modelling and fracture criterion. *Theoretical and Applied Fracture Mechanics*. 2019; 102: 83–97.
47. Dunand M, Mohr D. On the predictive capabilities of the shear modified Gurson and the modified Mohr–Coulomb fracture models over a wide range of stress triaxialities and Lode angles. *Journal of the Mechanics and Physics of Solids*. 59(7): 1374–94.

48. Tu S, Ren X, He J, Zhang Z. Stress–strain curves of metallic materials and post-necking strain hardening characterization: A review. *Fatigue & Fracture of Engineering Materials & Structure*. 2020; 43(1): 3–19.
49. Neimitz A, Gałkiewicz J, Dzioba I. Calibration of constitutive equations under conditions of large strains and stress triaxiality. *Archives of Civil and Engineering Materials*. 2018; 18: 1123–35.
50. ABAQUS 6.12. ABAQUS/Standard User’s Manual, Version 6.12 [Internet]. Dassault Systèmes Simulia Corp; 2020. Dostępne na: <http://130.149.89.49:2080/v6.12/index.html>
51. Dzioba I, Lipiec S. Fracture Mechanisms of S355 Steel—Experimental Research, FEM Simulation and SEM Observation. *Materials*. styczeń 2019; 12(23): 3959.
52. Ritchie RO, Knott JF, Rice JR. On the relationship between critical tensile stress and fracture toughness in mild steel. *Journal of the Mechanics and Physics of Solids*. 1973; 21: 395–410.
53. Neimitz A, Graba M, Gałkiewicz J. An alternative formulation of the Ritchie-Knott-Rice local fracture criterion. *Engineering Fracture Mechanics*. 2007; 74(8): 1308–22.
54. Fincato R, Yonezawa T, Tsutsumi S. Numerical modeling of cyclic softening/hardening behavior of carbon steels from low- to high-cycle fatigue regime. *Archives of Civil and Mechanical Engineering*. 2023; 23(3).
55. Bao Y, Wierzbicki T. On fracture locus in the equivalent strain and stress triaxiality space. *International Journal of Mechanical Sciences*. 2004; 46(1): 81–98.
56. Neimitz A, Dzioba I, Lipiec S. Calibration of constitutive equations for the stress level estimation in domain with the large strains. *Procedia Structural Integrity*. 2018; 13: 862–7.